PROCEEDINGS A

royalsocietypublishing.org/journal/rspa

Research

Cite this article: Al Saadi F, Gai C, Nelson M. 2024 Localized pattern formation: semi-strong interaction asymptotic analysis for three components model. *Proc. R. Soc. A* **480**: 20230591.
https://doi.org/10.1098/rspa.2023.0591

Received: 14 August 2023
Accepted: 24 November 2023

Subject Areas:
pattern recognition

Keywords:
reaction–diffusion, pattern formation, localized structures, breather pattern

Author for correspondence:
Fahad Al Saadi
e-mail: fahad.alsaadi@mtc.edu.om

Localized pattern formation: semi-strong interaction asymptotic analysis for three components model

Fahad Al Saadi[1,2], Chunyi Gai[3] and Mark Nelson[4]

[1]Department of Systems Engineering, Military Technological College, Muscat, Oman
[2]Department of Engineering Mathematics, University of Bristol, Bristol BS8 1UB, UK
[3]Mathematics Department, University of British Colombia, Vancouver, Canada
[4]School of Mathematics and Applied Statistics, University Of Wollongong, Wollongong, Australia

FAS, 0000-0003-4269-0137

We investigate a three-component system involving the Belousov–Zhabotinsky reaction in water-in-oil microemulsions. Our goal is to investigate the connection between homoclinic snaking and semi-strength interaction in a three-variable reaction–diffusion system. A two-parameter bifurcation diagram of homogeneous, periodic and localized patterns is obtained numerically, and a natural asymptotic scaling for semi-strong interaction theory is found where an activator source term $a = O(\delta_1)$ and $b = O(\delta_1)$, with $\delta_1 \ll 1$ being the diffusion ratio. Under this regime, singular perturbation techniques are used to construct localized steady-state patterns, and new types of non-local eigenvalue problems (NLEP) are derived to determine the stability of these patterns to $O(1)$ time-scale instabilities. We extend the scope of the NLEP by considering a general scenario where both time-scaling parameters are non-zero. All analytical results are found to agree with numerics. Further numerical results are presented on the location of various types of breathing Hopf instability for localized patterns.

1. Introduction

Oscillatory processes are ubiquitous in living systems, making them a fundamental aspect of biological

phenomena. Consequently, physical chemists have long championed the idea that chemical oscillators can be used for understanding biological oscillators [1]. A well-known chemical system is the Belousov–Zhabotinsky reaction (BZ), which involves the periodic oxidation of malonic acid by bromate in an acidic aqueous solution. It has been widely used as a model to study the emergence and behaviour of self-organizing systems that are of great biological significance.

In order to provide the best analogues to living cells, it is essential to investigate chemical oscillators within microheterogeneous environments rather than homogeneous ones. One particular type of such media is obtained by dispersing nanosized water droplets, each surrounded by a surfactant monolayer, into a continuous oil (octane) phase. A widely studied water-in-oil microemulsion uses the surfactant Aerosol OT, a.k.a sodium bis(2-ethylhexyl)-sulfosuccinate. The resulting media is known as the AOT microemulsion. An attractive feature of this system is that its microstructure can be tuned by changing the concentration and size of the water droplets [2].

The BZ reaction in water-in-oil microemulsions (BZ-AOT systems) has been extensively studied and has revealed a remarkable abundance of diverse waves and patterns [3,4]. In [5], Yang *et al*. investigated two models for the BZ reaction in an AOT microemulsion (BZ-AOT system). These models extend the standard Brusselator [6] and Oregonator [7] models by allowing the activator species to reversibly transform into an unreactive rapidly diffusing species. The introduction of a rapidly diffusing activator allows the extended system to exhibit wave instabilities. Yang *et al*. [5] show that the interaction of the stationary Turing and wave (oscillatory Turing) instabilities leads to a large variety of spatio-temporal patterns.

In this paper, we consider the extended Brusselator model for the BZ-AOT system proposed by Yang *et al*. [5], which takes the form

$$\frac{\partial u}{\partial t} = a - (b+1)u + u^2 v - cu + dw + \delta_1 \frac{\partial^2 u}{\partial x^2}, \quad x \in (-l, l),\ t > 0, \tag{1.1a}$$

$$\frac{\partial v}{\partial t} = bu - u^2 v + \frac{\partial^2 v}{\partial x^2}, \quad x \in (-l, l),\ t > 0 \tag{1.1b}$$

and

$$\frac{\partial w}{\partial t} = cu - dw + \delta_2 \frac{\partial^2 w}{\partial x^2}, \quad x \in (-l, l),\ t > 0, \tag{1.1c}$$

with boundary conditions

$$u_x|_{\partial\Omega} = v_x|_{\partial\Omega} = w_x|_{x=\partial\Omega} = 0.$$

Here, u, v and w are dimensionless variables representing the activator, inhibitor and unreactive species, respectively. The dimensionless parameters $\delta_1 > 0$, $\delta_2 > 0$ measures the ratio of the diffusion rate of the activator u to that of the inhibitor v and the ratio of the diffusion rate of the unreactive w to that of the inhibitor v. In what follows, we shall be interested in the case that $\delta_2 = \delta_1^2$ and in the limit of an infinitely long domain $l \to \infty$, while the parameters a, b, c and d are positive constants. In recent years, there has been a growing interest in studying the formation and dynamics of spatially localized patterns in reaction–diffusion systems. One particularly fascinating phenomenon in this field is known as homoclinic snaking, which gives rise to the emergence of localized states with arbitrarily wide spatial extent within the Pomeau pinning region. This phenomenon has been observed in various physical systems, including shear flows [8], fluid convection [9], neurons [10], water waves [11] and reaction–diffusion systems [12].

Furthermore, there has also been a recent focus on the generation of spike patterns in reaction–diffusion systems through the application of semi-strong interaction theory on infinite domains. Additionally, researchers have been focusing on assessing the stability of spike patterns using the non-local eigenvalue problem (NLEP). While the NLEP analysis has been applied to various three-component systems like the three-component Schnakenberg model [13], the urban crime model [14,15] and the extended vegetation model [16], most studies have only considered the impact of a single time-scaling parameter.

In this paper, we aim to expand upon our previous work by integrating homoclinic snaking theory and semi-strong interaction theory within a reaction–diffusion system that involves three components in one spatial dimension. Moreover, we extend the scope of the NLEP by considering a more general scenario where both time-scaling parameters, denoted as τ and θ, are positive (see equation (4.1)). This extended analysis necessitates new investigative approaches. To accomplish this, we re-investigate the extended Brusselator model (1.1).

The rest of the paper is organized as follows. Section 2 presents the linear stability analysis results of the system under investigation. In addition, a numerical overview is provided, highlighting the regions where periodic and localized patterns are observed. Building upon the linear stability analysis, §3 applies asymptotic analysis on a finite domain to construct spike patterns. This section also explores patterns when the domain size becomes infinite.

In §4, the stability of single-spike patterns is studied. This is accomplished by deriving a NLEP. To obtain a more general stability result of the NLEP, two parameters τ and θ are introduced as seen in equation (4.1). These parameters are associated with the timescales of the variables v and w. The complex behaviours of the NLEP are investigated by varying these parameters, offering insights into the dynamics of the system.

In §5, numerical results are presented on the location of various types of breathing Hopf instability for localized patterns. Finally, §6 draws conclusions and identifies the broader implications of the study.

2. Preliminaries

In this section, we investigate the linear stability of the homogeneous state in the system (1.1). By setting $u_t = v_t = w_t = 0$, system (1.1) admits a unique homogeneous steady state

$$(u_s, v_s, w_s) = \left(a, \frac{b}{a}, \frac{ac}{d}\right).$$

Now we investigate two of the main types of symmetry breaking bifurcation that can occur when the homogeneous steady-state loses stability, namely the Hopf bifurcation and the Turing instability bifurcation, which are responsible for the emergence of spatio-temporal patterns. To determine the conditions under which such bifurcations may occur, we carry out the linear stability analysis. The analysis is conducted by introducing new variables

$$(u, v, w) = (u_s, v_s, w_s) + (U, V, W), \tag{2.1}$$

and assuming an ansatz that

$$(U, V, W) = (\bar{U}, \bar{V}, \bar{W})e^{ikx+\lambda t} + c.c, \quad ||(\bar{U}, \bar{V}, \bar{W})|| \ll 1, \tag{2.2}$$

where k and λ indicate the wavenumber of the pattern and the rate of growth perturbation in time, respectively. By substituting (2.1) and (2.2) into (1.1), and ignoring the nonlinear terms, we obtain a linearized system which has the following characteristic equation:

$$|J - k^2 D - \lambda I| = 0. \tag{2.3}$$

Here, J is the Jacobian matrix, $D = \mathrm{diag}(\delta_1, 1, \delta_1^2)$ and I stands for the identity matrix.

Hopf bifurcation transforms a stationary steady state into spatially stationary and temporally periodic oscillations. This phenomenon arises when the following conditions are satisfied:

$$\Im(\lambda(k)) \neq 0, \quad \Re(\lambda(k)) = 0, \ k = 0. \tag{2.4}$$

The homogeneous steady-state solution of (1.1) loses stability at a spatial instability bifurcation to give solutions that are periodic in space but uniform in time when the following critical

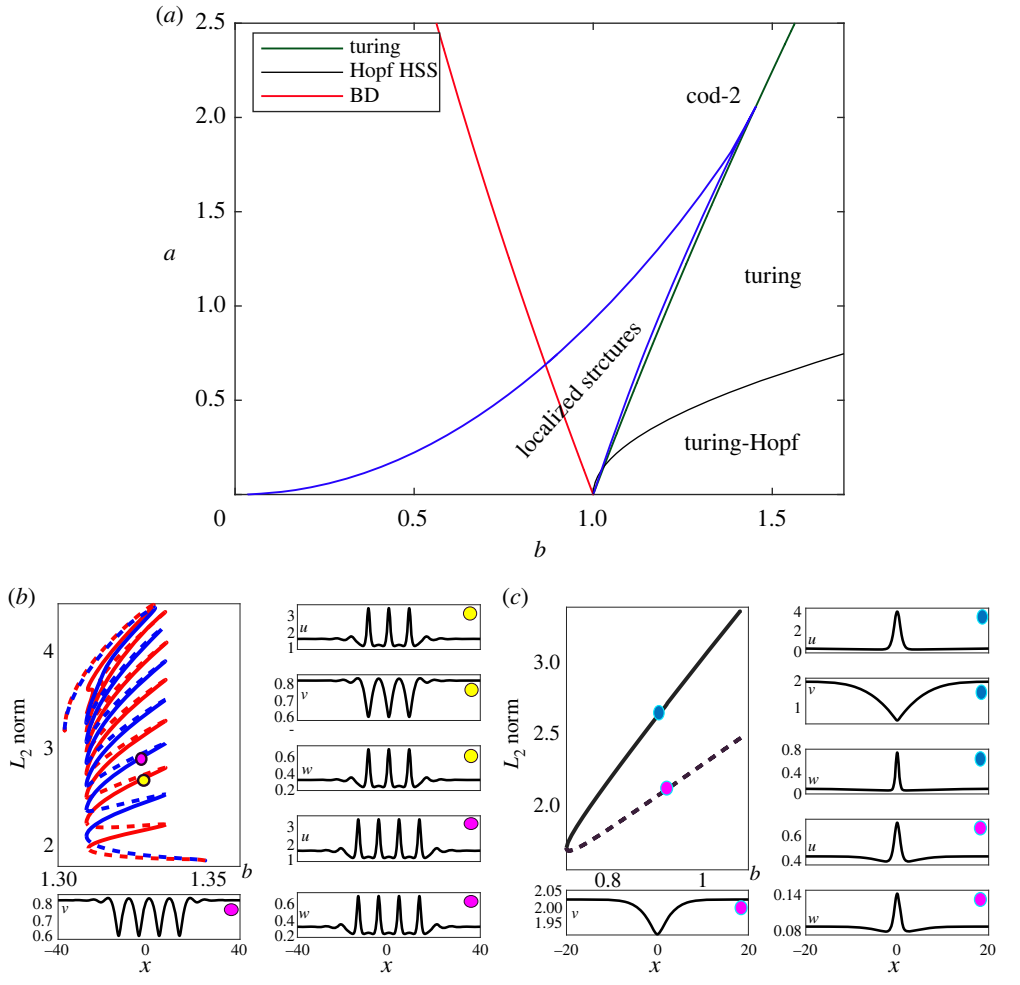

Figure 1. (*a*) Plane of (*b*,*d*) with $\delta_1 = 0.01$, $c = 0.2$ and $d = 1$, here the green indicates localized structures region, the red curve is Belyakov–Devaney (BD) transition and the green curve presents Turing instability. The black circle indicates the location of the codimension two point. (*b*) Bifurcation diagram shows the snaking ladder structure and samples of localized solution that are marks in the snaking with fixing $a = 1.7$ as b varies. The continuous (dashed) line indicates stable (unstable) solutions where the blue (red) line is the odd (even) solution branch. (*c*) The one parameter continuation along b in the spike region with fixing $a = 0.744$. The panel to the right shows example from the upper and lower branch indicated by light blue and magenta, respectively.

conditions are satisfied [17]:

$$\Re(\lambda(k))|_{k_c} = 0 \quad \text{and} \quad \partial_k \Re(\lambda(k))|_{k_c} = 0. \tag{2.5}$$

The value of the wavenumber (k) at which these conditions holds ($k = k_c$) is known as the critical value of the wavenumber.

Figure 1*a* shows the results of the linear stability analysis of (1.1) in the (a, b)-plane for fixed c, d and δ values of 0.2, 1 and 0.01, respectively. The green curve represents the critical Turing instability curve with a critical wavenumber greater than zero ($k_c > 0$). Hopf bifurcation of a homogeneous steady state (Hopf HSS) (black curve) divides the Turing region into two subregions, the stable Turing region (above) and the unstable Turing Hopf region (below).

The red curve in the figure represents another linear transition which is the Belyakov–Deveney (BD) transition, which occurs when the critical wavenumber is negative ($k_c < 0$). In the context of

spatial dynamics, [18] observes that this transition occurs when there is a pair of double real eigenvalues of a problem of (1.1).

Figure 1*a* also shows a codimension-2 point (shown as the black circle in the figure) which is obtained through weakly nonlinear analysis (details not included). Upon reaching this point, the Turing bifurcation shifts from subcritical to supercritical bifurcation. In the case of $a > 2$, the Turing bifurcation bifurcates supercritically as b increases, while it bifurcates subcritically for $a < 2$, as b decreases. Subcritical folds of periodic structures form a pinning region in the subcritical region where localized patterns can be observed. In our numerical calculations, we define the domain as $\Omega = (-l_x, l_x)$ where $l_x = 100$. We represent the norm using the following expressions:

$$L_2 \text{ norm} := \sqrt{\frac{1}{2l_x}\int_{-l_x}^{l_x}\sum_{i=1}^{4}(u_i(x))^2\,\mathrm{d}x} \quad \text{(for steady states)} \tag{2.6}$$

$$||u||_2 := \sqrt{\frac{1}{2Tl_x}\int_0^T\int_{-l_x}^{l_x}|u(x,t)|^2\,\mathrm{d}x\,\mathrm{d}t} \quad \text{(for time-periodic states).} \tag{2.7}$$

Here, we are only considering the first component, subtracting u^* (meaning that $||u||_2$ is not strictly a norm), and normalizing by both the domain size and, when dealing with time-periodic orbits, the period T.

By using AUTO, we obtain the localized patterns region, which can be seen as a blue envelope in figure 1*a*. This region is further divided into two subregions by the BD transition curve. Typically, the region to the right of the BD curve is where system (1.1) has spatially complex eigenvalues and localized pattern solutions that display an oscillation tail known as the sinking region. To the left of the BD curve, system (1.1) exhibits pure real eigenvalues and the localized pattern solution displays a montonic tail, which is also known as a spike region.

Figure 1*b*,*c* illustrates one parameter continuations from the snaking and spike regions, respectively. Figure 1*b* represents the standard homoclinic snake, which is composed of two intertwined branches of the localized patterns. The figure also illustrates the stability of each branch of the snaking diagram, which are determined numerically by using PDE2PATH [19,20]. The subplots are also used to show examples of localized pattern solutions at marked points in the snaking diagram.

Figure 1*c* illustrates a single fold that connects a stable branch to an unstable branch through a fold with examples from each branch plotted separately. Specifically, we note that the solution from the single fold has highly localized spikes in u and w, but is more dispersed in v. This observation suggests that the semi-strong asymptotic analysis may be used to effectively predict the solutions in the subplots of figure 1*c*. Recent studies have shown how to find the spike solution for a two-component model by using strong asymptotic analysis; in this study, we seek to extend the approach to a three-component model.

3. Semi-strong interaction asymptotic analysis

The procedure that we apply to find the spike equilibrium solution using asymptotic approximation is similar to that used in [21,22]. The first step is considering the steady-state system of (1.1)

$$a - (b+1)u + u^2v - cu + dw + \delta_1\frac{\partial^2 u}{\partial x^2} = 0, \tag{3.1a}$$

$$bu - u^2v + \frac{\partial^2 v}{\partial x^2} = 0 \tag{3.1b}$$

and

$$cu - dw + \delta_1^2\frac{\partial^2 w}{\partial x^2} = 0, \tag{3.1c}$$

subject to Neumman boundary conditions $u_x(\pm l) = v_x(\pm l) = w_x(\pm l) = 0$. Our focus is on the case in which $l \to \infty$. At this point, we shall seek a solution for (3.1) which is homoclinic in space to

the homogeneous steady state

$$u \to a, \quad v \to \frac{b}{a}, \; w \to \frac{ac}{d} \text{ as } x \to \pm l.$$

We are interested in small values of the parameters to be able to apply semi-strong interaction asymptotic. Therefore, we introduce a new scale for a and b as following

$$a = \delta_1 \alpha, \quad b = \delta_1 \beta \text{ with } \delta_1 \ll 1.$$

Substituting the above scale in the steady-state problem we gain the following system:

$$\delta_1 \alpha - (\delta_1 \beta + 1)u + u^2 v - cu + dw + \delta_1 \frac{\partial^2 u}{\partial x^2} = 0, \tag{3.2a}$$

$$\delta_1 \beta u - u^2 v + \frac{\partial^2 v}{\partial x^2} = 0 \tag{3.2b}$$

and

$$cu - dw + \delta_1^2 \frac{\partial^2 w}{\partial x^2} = 0. \tag{3.2c}$$

In the limit $\delta_1 \to 0$, we apply the matched asymptotic expansions to construct a single spike equilibrium centred at $x = 0$ of the system (3.2).

(a) Inner solution

As a starting point, we introduce a new inner spatial coordinate

$$x = \sqrt{\frac{\delta_1}{1 + \delta_1 \beta}}\, y. \tag{3.3}$$

Note that in the limit $\delta_1 \to 0$, both $a = \delta_1 \alpha \ll 1$ and $b = \delta_1 \beta \ll 1$ in (3.2*a*) and can be ignored to leading order. However, due to the fact that the localized structure region could admit slightly large b while keeping a small (see the lower left corner of the localized region of figure 1*a*), in this section, we choose to keep the $\delta_1 \beta$ term for better approximation of the steady state, so that the result is still accurate even if $\delta_1 \beta$ is not too small. This result will be used in the later §4(e) to be verified with numerical results. After collecting the leading order terms of system (3.2), we obtain the following system:

$$u_{yy} - u + \frac{u^2 v}{1 + \delta_1 \beta} = 0, \tag{3.4a}$$

$$v_{yy} = 0, \quad -\infty < y < \infty \tag{3.4b}$$

and

$$w = \frac{cu}{d}. \tag{3.4c}$$

We first solve the v-equation (3.4*b*). In order to match an outer solution, we require that $v(y)$ is bounded as $|y| \to \infty$. In this way, we obtain that $v(y) = v(0) = \kappa$ is a constant independent of y in the inner region. Then, from the u-equation, we let

$$u = \frac{1 + \delta_1 \beta}{\kappa} u_c(y), \tag{3.5}$$

where $u_c(y)$ satisfies

$$u_c'' - u_c + u_c^2 = 0, \quad -\infty < y < \infty \tag{3.6a}$$

and

$$u_c \to 0 \quad \text{as } y \to \pm\infty; \; u_c'(0) = 0, \; u_c(0) > 0. \tag{3.6b}$$

The solution to (3.6) is

$$u_c(y) = \frac{3}{2} \operatorname{sech}^2\left(\frac{y}{2}\right). \tag{3.7}$$

Hence,

$$w(y) = \frac{3c(1+\delta_1\beta)}{2d\kappa}\operatorname{sech}^2\left(\frac{y}{2}\right). \tag{3.8}$$

(b) Outer solution

To determine the constant κ, we consider the outer region, which is defined away from $O(\sqrt{\delta_1/(1+\delta_1\beta)})$ regions near $x=0$. First, we introduce new variables given as

$$u = \delta_1\hat{u}, \quad v = \hat{v},\ w = \delta_1\hat{w},\ x = \frac{z}{\delta_1}. \tag{3.9}$$

Once we introduce (3.9) into (3.2) we find that, to leading order,

$$\hat{u}(z) = \frac{\alpha}{1+\delta_1\beta}, \quad \hat{v}_{zz} - \hat{u}^2\hat{v} + \beta\hat{u} = 0, \text{ and } \hat{w}(z) = \frac{c\hat{u}(z)}{d}.$$

Note that $\hat{u}$ can be approximated as a multiple of delta functions due to the fact that it is localized near $x=0$. To solve the outer solution for $\hat{v}$, we integrate the $\hat{v}$-equation over $(0^-, 0^+)$ to obtain the following jump condition, where $(0^-, 0^+)$ is defined as a small interval that is slightly larger than the inner region:

$$\begin{aligned} S := \hat{v}_z(0^+) - \hat{v}_z(0^-) &= \int_{0^-}^{0^+} \hat{u}^2\hat{v}\,\mathrm{d}z - \beta\int_{0^-}^{0^+}\hat{u}\,\mathrm{d}z \\ &= \frac{6}{\kappa}\frac{\sqrt{1+\delta_1\beta}}{\sqrt{\delta_1}}. \end{aligned}$$

Here, we have used the fact that $\int_{-\infty}^{\infty} u_c(y)dy = \int_{-\infty}^{\infty} u_c^2(y)dy = 6$. Then in outer region $\hat{v}$ satisfies

$$\left.\begin{aligned} &\hat{v}_{zz} + \frac{\alpha\beta}{1+\delta_1\beta} - \frac{\alpha^2}{(1+\delta_1\beta)^2}\hat{v} = S\delta(z), \\ &\hat{v}_z(0^+) - \hat{v}_z(0^-) = S \\ \text{and} \quad &\hat{v}_z(\pm\delta_1 l) = 0. \end{aligned}\right\} \tag{3.10}$$

To solve system (3.10), we introduce Green's function $G(z)$ which satisfies

$$\left.\begin{aligned} &\frac{(1+\delta_1\beta)^2}{\alpha^2}G_{zz} - G = -\delta(z) \\ \text{and} \quad &G_z(\pm\delta_1 l) = 0. \end{aligned}\right\} \tag{3.11}$$

A simple calculation gives

$$G(z) = \frac{\alpha}{2(1+\delta_1\beta)}\frac{\cosh((\alpha/(1+\delta_1\beta))(\delta_1 l - |z|))}{\sinh((c\alpha/(1+\delta_1\beta))\delta_1 l)}. \tag{3.12}$$

The solution to (3.10) is then given by

$$\begin{aligned} \hat{v}(z) &= \frac{\beta(1+\delta_1\beta)}{\alpha} - \frac{S(1+\delta_1\beta)^2}{\alpha^2}G(z) \\ &= \frac{\beta(1+\delta_1\beta)}{\alpha} - \frac{3(1+\delta_1\beta)^{3/2}}{\kappa\alpha\sqrt{\delta_1}}\frac{\cosh((\alpha/(1+\delta_1\beta))(\delta_1 l - |z|))}{\sinh((\alpha/(1+\delta_1\beta))\delta_1 l)}, \end{aligned} \tag{3.13}$$

where κ is to be determined.

Note that in the large domain case where $l \to \infty$, (3.13) can be simplified as

$$\hat{v}(z) = \frac{\beta(1+\delta_1\beta)}{\alpha} - \frac{3(1+\delta_1\beta)^{3/2}}{\kappa\alpha\sqrt{\delta_1}}e^{-(\alpha/(1+\delta_1\beta))|z|}. \tag{3.14}$$

(c) Matching

To determine κ we match inner with outer solutions and take $z=0$ in equation (3.13) to obtain the following quadratic equation:

$$\kappa^2-\frac{\beta(1+\delta_1\beta)}{\alpha}\kappa+\frac{3(1+\delta_1\beta)^{3/2}}{\alpha\sqrt{\delta_1}\tanh((\alpha/(1+\delta_1\beta))\delta_1 l)}=0. \tag{3.15}$$

The equation has two solutions when the discriminant $\Delta=\beta^2(1+\delta_1\beta)^2/\alpha^2-(12(1+\delta_1\beta)^{3/2}/(\alpha\sqrt{\delta_1}\tanh((\alpha/(1+\delta_1\beta))\delta_1 l))>0$,

$$\kappa_\pm=\frac{\beta(1+\delta_1\beta)}{2\alpha}\pm\sqrt{\frac{\beta^2(1+\delta_1\beta)^2}{4\alpha^2}-\frac{3(1+\delta_1\beta)^{3/2}}{\alpha\sqrt{\delta_1}\tanh((\alpha/(1+\delta_1\beta))\delta_1 l)}}. \tag{3.16}$$

It has a fold point that occurs when $\Delta=0$:

$$\sqrt{1+\delta_1\beta}\sqrt{\delta_1}\tanh\left(\frac{\alpha}{1+\delta_1\beta}\delta_1 l\right)\beta^2=12\alpha. \tag{3.17}$$

We now summarize the results for one-spike steady states as follows:

Result 3.1. In the limit $\delta_1\to 0$, system (3.2) admits a one-spike steady-state solution centred at $x=0$, the steady state is given by

$$u_e\sim\frac{1+\delta_1\beta}{\kappa}u_c\left(\frac{\sqrt{1+\delta_1\beta}}{\sqrt{\delta_1}}x\right),\ \text{if } x=\mathcal{O}\left(\frac{\sqrt{\delta_1}}{\sqrt{1+\delta_1\beta}}\right);\ u_e\sim\frac{\delta_1\alpha}{1+\delta_1\beta}\ \text{otherwise,} \tag{3.18a}$$

$$v_e\sim\frac{\beta(1+\delta_1\beta)}{\alpha}-\frac{3(1+\delta_1\beta)^{3/2}}{\kappa\alpha\sqrt{\delta_1}}\frac{\cosh((\delta_1\alpha/(1+\delta_1\beta))(l-|x|))}{\sinh((\alpha/(1+\delta_1\beta))\delta_1 l)} \tag{3.18b}$$

and

$$w_e\sim\frac{c}{d}u_e, \tag{3.18c}$$

where κ satisfies the quadratic equation (3.15). Here, $u_c(y)=(3/2)\mathrm{sech}^2(y/2)$ is the homoclinic solution of (3.6).

In the large domain case where $l\to\infty$, $\tanh((\alpha/(1+\delta_1\beta))\delta_1 l)\to 1$, to leading order (3.15) reduces to

$$\kappa^2-\frac{\beta}{\alpha}\kappa+\frac{3}{\alpha\sqrt{\delta_1}}=0, \tag{3.19}$$

which can be written as the following in terms of the original parameters a,b:

$$a\kappa^2-b\kappa+3\sqrt{\delta_1}=0. \tag{3.20}$$

We then use the regular perturbation analysis to write the approximation of the two roots in terms of original parameters a,b

$$\kappa_1\approx\frac{3\sqrt{\delta_1}}{b}+\frac{9a\delta_1}{b^3} \tag{3.21a}$$

and

$$\kappa_2\approx\frac{b}{a}-\frac{3\sqrt{\delta_1}}{b}. \tag{3.21b}$$

Here, the above two values of κ are corresponding to the value of κ in the upper branch (κ_1) and the lower branch (κ_2). Moreover, the discriminant of (3.20) which is given as

$$b^2-12\,a\sqrt{\delta_1}=0, \tag{3.22}$$

provides the curve of the localized structure in the spike region. In the panel in figure 2, we compare the curve that is obtained from (3.22) (red dashed) with the curve obtained from AUTO (solid blue) for the spike region.

Figure 3 compares the solution obtained by the semi-strong analysis with a numerical solution obtained by AUTO. It shows that the analysis result has a good agreement with the numerical solutions.

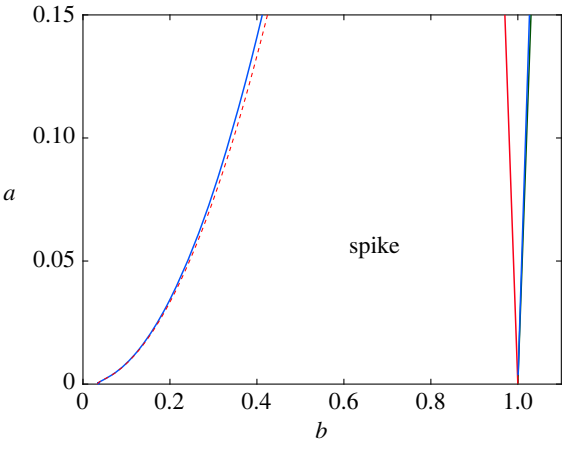

Figure 2. Zoom of the spike region of (1.1) for $\delta_1 = 0.01$. The analytical approximation of the fold bifurcation of the spike region is represented by the red dashed lines, while numerical computation by AUTO is represented by solid blue lines.

4. Stability analysis of single spike solutions

We now study the stability of one-spike equilibrium solutions to (3.2). We will start by considering a more general case where it is assumed that the timescales of the three fields could be different. In particular, two reaction-time scaling parameters θ, τ are added in front of v_t, w_t, respectively, so that system (3.2) becomes

$$\left.\begin{aligned} u_t &= \delta_1 \frac{\partial^2 u}{\partial x^2} + u^2 v - cu + dw + \delta_1 \alpha - (\delta_1 \beta + 1)u, \\ \theta v_t &= \frac{\partial^2 v}{\partial x^2} - u^2 v + \delta_1 \beta u \\ \text{and} \qquad \tau w_t &= \delta_1^2 \frac{\partial^2 w}{\partial x^2} + cu - dw. \end{aligned}\right\} \tag{4.1}$$

Firstly, upon introducing the perturbation around the steady state

$$\left.\begin{aligned} u(x,t) &= u_e(x) + \phi(x)\, \mathrm{e}^{\lambda t}, \\ v(x,t) &= v_e(x) + \psi(x)\, \mathrm{e}^{\lambda t} \\ \text{and} \qquad w(x,t) &= w_e(x) + \xi(x)\, \mathrm{e}^{\lambda t}, \end{aligned}\right\} \tag{4.2}$$

where $|\phi|, |\psi|, |\xi| \ll 1$, we obtain the following linearized eigenvalue problem for ϕ, ψ and ξ

$$\left.\begin{aligned} \lambda \phi &= \delta_1 \phi_{xx} + 2u_e v_e \phi + u_e^2 \psi - c\phi + d\xi - (\delta_1 \beta + 1)\phi, \\ \theta \lambda \psi &= \psi_{xx} - 2u_e v_e \phi - u_e^2 \psi + \delta_1 \beta \phi \\ \text{and} \qquad \tau \lambda \xi &= \delta_1^2 \xi_{xx} + c\phi - d\xi \end{aligned}\right\} \tag{4.3}$$

with Neumann boundary conditions on the finite domain $(-l, l)$.

The spectrum of (4.3) contains two classes of eigenvalues. There are 'large' eigenvalues that are $O(1)$ and 'small' eigenvalues that approach 0 as $\delta_1 \to 0$. As one-spike equilibrium is stable with respect to small eigenvalues (see [23,24] for more details), in this section, we will analyse the 'large' $O(1)$ eigenvalues in the spectrum of the linearization.

In the limit $\delta_1 \to 0$, the effect of the higher order term $\delta_1 \beta$ in this section will not be considered when solving the eigenvalue problem (4.3). Then to leading order the steady state u_e, v_e and w_e is

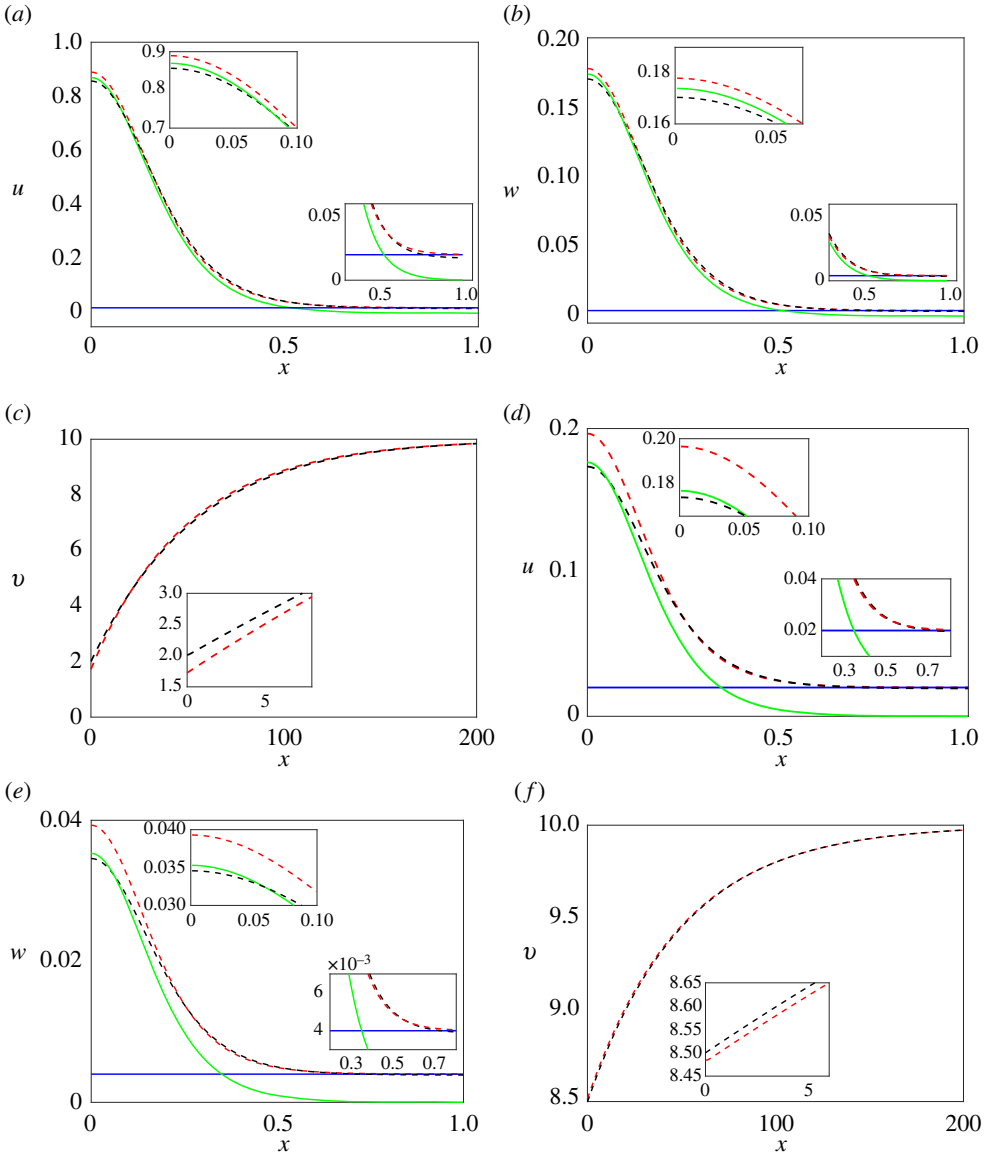

Figure 3. A comparison of the approximation solution which obtained by the semi-strong analysis with the full numerical solution from AUTO for the upper and lower branch for $a = 0.02$, $b = 0.2$, $c = 0.2$, $d = 1$, $\delta_1 = 0.01$ and $L = 1000$. (*a–c*): the solution of u, w and v for the stable branch, respectively, with $\kappa = 1.725$ obtained from (3.21*a*). In (*a*,*b*,*d*,e), the green and blue continuous lines represent the inner and the outer solution, respectively, and the red (black) dashed line indicates the asymptomatic (numerical) solution. (*d–f*): The approximate and the numerical solution of u, w and v in the unstable branch is shown with $\kappa = 8.5$ obtained from (3.21*b*), respectively, where the colour code is similar to that in the stable branch.

given as below

$$\left.\begin{aligned} u_e &\sim \frac{1}{\kappa} u_c\left(\frac{x}{\sqrt{\delta_1}}\right), \text{ if } x = \mathcal{O}\left(\sqrt{\delta_1}\right); \; u_e \sim \delta_1 \alpha \text{ otherwise,} \\ v_e &\sim \frac{\beta}{\alpha} - \frac{3}{\kappa\alpha\sqrt{\delta_1}} \frac{\cosh(\delta_1\alpha(l-|x|))}{\sinh(\alpha\delta_1 l)} \\ \text{and} \quad w_e &\sim \frac{c}{d} u_e, \end{aligned}\right\} \tag{4.4}$$

where κ satisfies

$$\kappa^2 - \frac{\beta}{\alpha}\kappa + \frac{3}{\alpha\sqrt{\delta_1}\tanh(\alpha\delta_1 l)} = 0. \tag{4.5}$$

The asymptotic analysis as $\delta_1 \to 0$ proceeds as follows. In the inner region, we introduce an inner variable $y = x/\sqrt{\delta_1}$, then to leading order we obtain $\psi_{yy} = 0$. Imposing Neumann boundary conditions, we get $\psi \sim \psi_0$ is a constant that is to be determined. Moreover, collecting leading orders in the ξ-equation, we obtain that $\tau\lambda\xi = c\phi - d\xi$, which yields

$$\xi = \frac{c}{\tau\lambda + d}\phi. \tag{4.6}$$

Then using (4.6) to remove ξ yields the following equation for ϕ:

$$\lambda\left(1 + \frac{\tau c}{\tau\lambda + d}\right)\phi = \phi_{yy} + 2u_c\phi - \phi + \frac{u_c^2}{\kappa^2}\psi_0. \tag{4.7}$$

To compute the constant ψ_0, we look at the outer region. Since in the outer region, the localized spike can be approximated as a multiple of delta functions, so ψ satisfies

$$\psi_{xx} - \theta\lambda\psi - \delta_1^2\alpha^2\psi = c\delta(x;0), \tag{4.8}$$

where

$$\begin{aligned} c &= 2\int_{0^-}^{0^+} u_e v_e\phi \,\mathrm{d}x + \int_{0^-}^{0^+} u_e^2\psi \,\mathrm{d}x - \int_{0^-}^{0^+} \delta_1\beta\phi \,\mathrm{d}x \\ &\sim 2\sqrt{\delta_1}\int_{-\infty}^{\infty} u_c\phi \,\mathrm{d}y + \frac{6\sqrt{\delta_1}}{k^2}\psi_0 + O(\delta_1^{3/2}). \end{aligned} \tag{4.9}$$

Here, $(0^-, 0^+)$ is defined as a small interval that is slightly larger than the inner region, and we have used the fact that $\int_{0^-}^{0^+} u_e^2\psi dx = \sqrt{\delta_1}\psi_0\int_{-\infty}^{\infty} u_e^2 \,\mathrm{d}y = \psi_0(\sqrt{\delta_1}/\kappa^2)\int_{-\infty}^{\infty} u_c^2 \,\mathrm{d}y = (6\sqrt{\delta_1}/k^2)\psi_0$. We then write the solution to (4.8) in terms of Green's function as follows:

$$\psi = cG(x;\mu), \quad \mu := \sqrt{\theta\lambda + \delta_1^2\alpha^2}, \tag{4.10}$$

where $G(x;\mu)$ is Green's function which satisfies

$$\left.\begin{aligned} &G_{xx} - \mu^2 G = \delta(x;0) \\ \text{and} \quad &G_x(\pm l) = 0, \end{aligned}\right\} \tag{4.11}$$

and the solution is

$$G(x;\mu) = -\frac{1}{2\mu\sinh(\mu l)}\cosh(\mu(|x| - l)). \tag{4.12}$$

Therefore, the solution to (4.8) is

$$\psi(x) = -\frac{c}{2\mu\sinh(\mu l)}\cosh(\mu(|x| - l)), \tag{4.13}$$

where c and μ are given in (4.9) and (4.10), respectively. Then we determine ψ_0 by taking $x = 0$ in (4.13) and we obtain

$$\psi_0 = \psi(0) = -\frac{\sqrt{\delta_1}\int u_c\phi dy + \frac{3\sqrt{\delta_1}}{k^2}\psi_0}{\sqrt{\theta\lambda + \delta_1^2\alpha^2}\tanh(\sqrt{\theta\lambda + \delta_1^2\alpha^2}l)}, \tag{4.14}$$

which yields

$$\psi_0 = -\frac{\sqrt{\delta_1}\int \phi u_c \,\mathrm{d}y}{(3\sqrt{\delta_1}/\kappa^2) + \sqrt{\theta\lambda + \delta_1^2\alpha^2}\tanh(\sqrt{\theta\lambda + \delta_1^2\alpha^2}l)}. \tag{4.15}$$

Eventually, substituting (4.15) into (4.7) yields the following NLEP for ϕ:

$$\lambda\left(1 + \frac{\tau c}{\tau\lambda + d}\right)\phi = \phi_{yy} - \phi + 2u_c\phi - u_c^2\frac{\int \phi u_c dy}{A}, \tag{4.16}$$

royalsocietypublishing.org/journal/rspa Proc. R. Soc. A 480: 20230591

where we used the simplified notation $\int f dy := \int_{-\infty}^{\infty} f dy$ and

$$A = 3 + \sqrt{\frac{\theta\lambda}{\delta_1} + \delta_1\alpha^2}\tanh\left(l\sqrt{\theta\lambda + \delta_1^2\alpha^2}\right)\kappa^2. \tag{4.17}$$

We take τ and θ as bifurcation parameters to investigate their influence on stability. To make this, we consider the following different cases depending on the value of θ and τ: (1) $\tau = \theta = 0$; (2) $\tau > 0, \theta = 0$; (3) $\tau = 0, \theta > 0$; (4) $\tau > 0, \theta > 0$. The stability results in the two cases with $\tau = 0$ have essentially the same structure as the NLEP studied in [21]. The other two cases are new results. Here, we will look at all cases for completeness.

(a) Case 1: $\theta = 0, \tau = 0$.

We first consider the simplest case and take $\theta = 0, \tau = 0$, so that equation (4.16) reduces to the following well-known NLEP:

$$\lambda\phi = L_0\phi - u_c^2\frac{\int \phi u_c dy}{A} \quad \text{and} \quad A = 3 + \sqrt{\delta_1}\alpha\tanh(\delta_1\alpha l)\kappa^2, \tag{4.18}$$

in which $L_0\phi \equiv \phi_{yy} - \phi + 2u_c\phi$. This NLEP is first studied in [25]. It has the following basic result:

Theorem 4.1 (See [25]). *Consider the problem (4.18), let λ be an eigenvalue with largest real part that corresponds to an eigenfunction ϕ.*

(*i*) *If $A > 6$, then there exists λ with $\lambda > 0$.*
(*ii*) *If $A < 6$, then either $Re(\lambda) < 0$ or $\lambda = 0$ with the corresponding eigenfunction $\phi = u_c'(y)$.*
(*iii*) *If $A = 6$, then $\lambda = 0$ with $\phi = u_c$.*

To determine the stability of the two branches κ_- and κ_+ shown in (4.5), we substitute $\kappa_\pm$ into (4.18) to obtain

$$A(\kappa_\pm) = \frac{\sqrt{\delta_1}\beta^2\tanh(\delta_1\alpha l)}{2\alpha} \pm \frac{\beta\sqrt{\tanh(\delta_1\alpha l)}}{2\alpha^{1/2}}\sqrt{\frac{\beta^2\sqrt{\delta_1}\tanh(\delta_1\alpha l)}{\alpha} - 12}. \tag{4.19}$$

Since existence of the roots $\kappa_\pm$ requires $\sqrt{\delta_1}\beta^2\tanh(\delta_1\alpha l)/\alpha > 12$, it is easy to see that $A(\kappa_+) > 6$, so by theorem 4.1, we obtain that the upper branch $\kappa = \kappa_+$ is unstable. For the other branch $\kappa = \kappa_-$, we take $\sqrt{\delta_1}\beta^2\tanh(\delta_1\alpha l)/\alpha = 12 + \eta$, where $\eta > 0$, then we can rewrite $A(\kappa_-)$ as

$$A(\kappa_-) = 6 - \frac{\sqrt{12\eta + \eta^2} - \eta}{2} < 6. \tag{4.20}$$

Therefore, we conclude based on theorem 4.1 that the branch with $\kappa = \kappa_-$ is stable. Moreover, at the fold point where $\sqrt{\delta_1}\beta^2\tanh(\delta_1\alpha l)/\alpha = 12$, we can easily reduce (4.19) to $A = 6$, which corresponds to $\lambda = 0$.

(b) Case 2: $\tau > 0, \theta = 0$

In the case where $\tau > 0, \theta = 0$, (4.16) simplifies to the following equation:

$$\chi(\lambda)\phi = L_0\phi - u_c^2\frac{\int \phi u_c \, dy}{A}, \tag{4.21}$$

where

$$\chi(\lambda) = \lambda\left(1 + \frac{\tau c}{\tau\lambda + d}\right), \tag{4.22}$$

and A is independent of λ

$$A = 3 + \sqrt{\delta_1}\alpha\tanh(\delta_1\alpha l)k^2.$$

Note that equation (4.21) is similar to the well-known NLEP (4.18) except that the left-hand side of equation (4.21) is a function of λ instead of λ alone. To understand the effect of τ on the stability of the system, we need to figure out how the eigenvalue λ relates to the function $\chi(\lambda)$.

royalsocietypublishing.org/journal/rspa Proc. R. Soc. A 480: 20230591

First we rewrite equation (4.22) as a quadratic equation in terms of λ,

$$\tau\lambda^2 + (\tau c + d - \tau\chi)\lambda - \chi d = 0. \tag{4.23}$$

This equation satisfies the following properties (see proof in appendix A):

Lemma 4.2. *Consider the quadratic equation (4.23) with $\tau, c, d > 0$. Then*

(*i*) *When χ is real and positive, the equation has two real roots and their signs are opposite; when χ is real and negative, then equation (4.23) has either two negative real roots or two complex roots with $Re(\lambda) < 0$; when $\chi = 0$, then equation (4.23) has two roots $\lambda_1 = 0, \lambda_2 = -((\tau c + d)/\tau) < 0$.*
(*ii*) *When τ is complex and $Re(\chi) \le 0$, then the roots of equation (4.23) have negative real parts: $Re(\lambda) < 0$.*

Now we consider the stability of the two branches. For the upper branch $\kappa = \kappa_+$, we have shown in §4(a) that $A(k_+) > 6$ when $\tau = \theta = 0$, so based on theorem 4.1 and lemma 4.2, there exists χ with $\chi > 0$, which means a real positive eigenvalue ($\lambda > 0$) exists for the NLEP (4.21). Therefore, the upper branch with $\kappa = \kappa_+$ is unstable.

On the other hand, when $\kappa = \kappa_-$, we have $A(\kappa_-) < 6$, and according to theorem 4.1 and lemma 4.2, we conclude that $Re(\chi) < 0$ or $\chi = 0$ with $\phi = u_c'$, in the two cases we have $Re(\lambda) < 0$ or $\lambda = 0$, which shows that the lower branch $\kappa = \kappa_-$ is always stable. We now summarize the stability results for case 1 and case 2 as follows:

Result 4.3. Consider the system (4.1) with $\theta = 0$, $\tau \ge 0$, the one-spike equilibrium $u_e(x), v_e(x), w_e(x)$ given in (4.4), with $v_0 = k_+$ is unstable and the other branch $v_0 = k_-$ is always stable. The two roots connect at a fold point corresponding to a double root of (4.5).

From result 4.3, we see that in the limit $\delta_1 \to 0$, changing the value of τ alone does not affect the fold bifurcation structure.

(c) Case 3: $\tau = 0, \theta > 0$

When choosing $\theta > 0$ and $\tau = 0$, the NLEP (4.16) simplifies to

$$\lambda\phi = L_0\phi - u_c^2 \frac{\int \phi u_c \, dy}{A(\lambda)}, \tag{4.24}$$

where $L_0\phi = \phi_{yy} - \phi + 2u_c\phi$, and

$$A(\lambda) = 3 + \sqrt{\delta_1\alpha^2 + \frac{\theta\lambda}{\delta_1}} \tanh\left(\sqrt{\theta\lambda + \delta_1^2\alpha^2} l\right) \kappa^2. \tag{4.25}$$

Equation (4.24) has a similar structure to the NLEP studied in [21]. Here, we use the same idea in [21] to derive the stability result of our model. First, we write (4.24) in the following form:

$$(L_0 - \lambda)\phi = u_c^2, \quad \text{where } \int \phi u_c \, dy = A(\lambda),$$

or

$$f(\lambda) := \int u_c (L_0 - \lambda)^{-1} u_c^2 \, dy = A(\lambda). \tag{4.26}$$

The global behaviour of this same $f(\lambda)$ was studied in [24], from which we obtain the following basic results:

Theorem 4.4 (See [24]). *$f(\lambda)$ has the behaviour*

$$f(0) = 6, f'(\lambda) > 0, f''(\lambda) > 0, \lambda \in \left(0, \frac{5}{4}\right).$$

Moreover, $f(\lambda)$ has a singularity at $\lambda = 5/4$ with $f(\lambda) \to \pm\infty$ as $\lambda \to 5/4_\pm$. For $\lambda > 5/4$, we have $f(\lambda) < 0$ and $f(\lambda) \to 0$ as $\lambda \to \infty$.

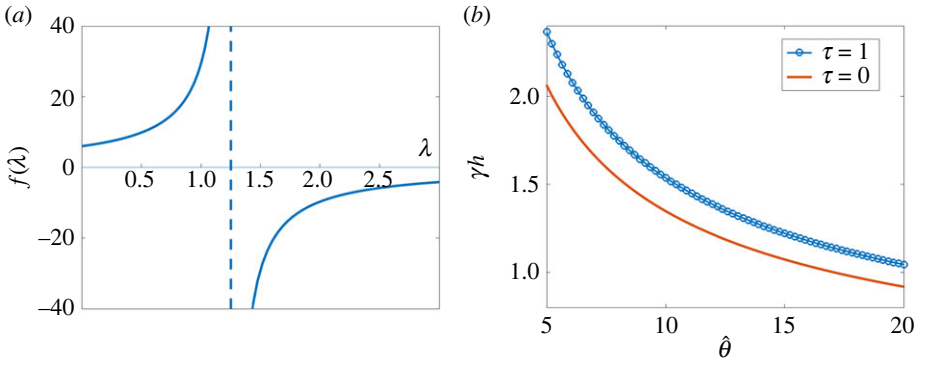

Figure 4. Computational results illustrating the stability analysis; (*a*) the function $f(\lambda)$ given in (4.26) and it has a singularity at $\lambda = 5/4$. (*b*) Hopf bifurcation points γ_h against $\hat{\theta}$ with $\tau = 0$ and $\tau = 1$ separately.

The graph of $f(\lambda)$ is shown in figure 4*a*. We then first study the stability of the upper branch $v_0 = \kappa_+$. Since $A(\lambda)$ on the right-hand side of equation (4.26) is continuous, and from §4(a) we have shown that $A(\lambda = 0, \kappa = \kappa_+) > 6$. Therefore, the two functions $f(\lambda)$ and $A(\lambda)$ must intersect in the domain $\lambda > 0$, so that equation (4.26) must have a positive real eigenvalue, which shows that the upper branch with $v_0 = \kappa_+$ is unstable.

We now study the stability of the other branch $v_0 = \kappa_-$. Since we are interested in large domain $l \to \infty$, so $\tanh(\delta_1 \alpha l) \sim 1$, then we rewrite $A(\lambda)$ as follows by introducing $\hat{\theta} := \theta/\delta_1^2\alpha^2$, and $\gamma := \kappa^2\sqrt{\delta_1\alpha^2}$:

$$A(\lambda) \sim 3 + \gamma\sqrt{\hat{\theta}\lambda + 1}. \tag{4.27}$$

When γ is sufficiently large, the system can be destabilized via a Hopf bifurcation. This result was first proved in [24]. Although there is no explicit formula for the threshold γ_h at which the Hopf bifurcation occurs, the critical value γ_h can be computed numerically by discretizing the NLEP (4.24) using finite differences. This is shown in figure 4*b*, where we choose fixed $\hat{\theta}$, and use the above method to compute γ_h such that $Re(\lambda) = 0$.

(d) Case 4: $\tau > 0, \theta > 0$

In this section, we consider the most general case $\tau > 0$, $\theta > 0$, which yields the following NLEP:

$$\chi(\lambda)\phi = L_0\phi - u_c^2 \frac{\int \phi u_c dy}{A(\lambda)}, \tag{4.28a}$$

$$\text{where} \quad \chi(\lambda) = \lambda\left(1 + \frac{\tau c}{\tau\lambda + d}\right) \tag{4.28b}$$

and

$$A(\lambda) = 3 + \sqrt{\theta\lambda + \delta_1^2\alpha^2}\tanh\left(\sqrt{\theta\lambda + \delta_1^2\alpha^2}\, l\right)\frac{\kappa^2}{\sqrt{\delta_1}}. \tag{4.28c}$$

We write equation (4.28*a*) in the following form:

$$g(\lambda) := \int u_c(L_0 - \chi(\lambda))^{-1}u_c^2\, \mathrm{d}y = A(\lambda). \tag{4.29}$$

The only difference between $g(\lambda)$ and $f(\lambda)$ given in (4.26) in §(b) is that $g(\lambda)$ contains $\chi(\lambda)$ instead of λ alone, so we need to figure out how the function $\chi(\lambda)$ affects the global behaviour of $g(\lambda)$. From lemma 4.2, we have that when $\chi > 0$, there is one and only one positive root; moreover, $\mathrm{d}\chi/\mathrm{d}\lambda = 1 + (\tau cd/(\tau\lambda + d)^2) > 0$, so $\chi(\lambda)$ is one to one in the region $\lambda > 0$ and is monotone increasing. Combining this property with theorem 4.4, we obtain that $g(\lambda)$ has the same structure as $f(\lambda)$, and we summarize it as follows:

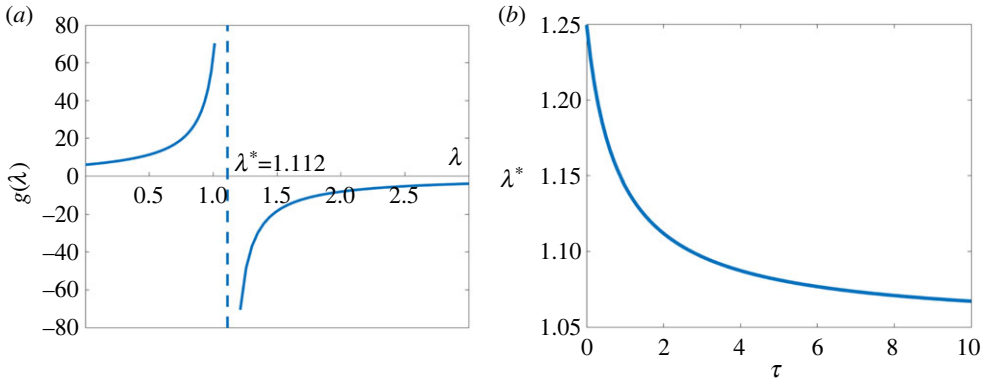

Figure 5. Computational results illustrating the stability analysis; (*a*) the function $g(\lambda)$ given in (4.29), here $\tau = 2, c = 0.2$, $d = 1$. (*b*) The graph of the singularity point λ^* in terms of τ. The other parameters are $c = 0.2, d = 1$.

Lemma 4.5. *$g(\lambda)$ has the behaviour*

$$g(0) = 6,\ g'(\lambda) > 0,\ g''(\lambda) > 0,\ \lambda \in (0, \lambda^*),$$

where $\lambda^* = (-(d + c\tau - (5/4)\tau) + \sqrt{(d + c\tau - (5/4)\tau)^2 + 5d\tau})/2\tau$ is the positive root of the equation

$$\lambda\left(1 + \frac{\tau c}{\tau\lambda + d}\right) = \frac{5}{4}.$$

Moreover, $g(\lambda)$ has a singularity at $\lambda = \lambda^*$, with $f(\lambda) \to \pm\infty$ as $\lambda \to \lambda^*_{\pm}$. For $\lambda > \lambda^*$, we have $g(\lambda) < 0$ and $g(\lambda) \to 0$ as $\lambda \to \infty$.

We plot the graph of $g(\lambda)$ in figure 5*a*, and in figure 5*b*, we plot the singularity point λ^* in terms of τ. Note that when $\tau = 0$, lemma 4.5 recovers the result in theorem 4.4.

We now study the stability of the two branches $v_0 = \kappa_{\pm}$ for $\tau > 0, \theta > 0$. Since the right-hand side of equation (4.29) $A(\lambda)$ is continuous with respect to λ, and it has been shown in §4(a) that $A(\lambda = 0, \kappa = \kappa_+) > 6 = g(0)$. Therefore, the two functions $g(\lambda)$ and $A(\lambda)$ must intersect in the domain $\lambda > 0$, so that equation (4.29) must have a real positive eigenvalue, which shows that the upper branch with $v_0 = \kappa_+$ is unstable.

For the other branch $v_0 = \kappa_-$, we first let $l \to \infty$ as we are interested in a large domain, so that $\tanh(\sqrt{\theta\lambda + \delta_1^2\alpha^2 l}) \to 1$, and $A(\lambda)$ can be simplified to

$$A(\lambda) \sim 3 + \gamma\sqrt{\hat{\theta}\lambda + 1}, \tag{4.30}$$

where

$$\gamma := \kappa^2\sqrt{\delta_1\alpha^2} \quad \text{and} \quad \hat{\theta} := \frac{\theta}{\delta_1^2\alpha^2}. \tag{4.31}$$

This scenario is similar to case 3 given in §4(c) but the stability is now dependent on the value of τ, and the system can be destabilized via a Hopf bifurcation when γ is large enough. We now summarize the stability results for case 3 and case 4 as the following result:

Result 4.6. In the case $\tau \geq 0$ and $\hat{\theta} > 0$, the one-spike solution $u_e(x), v_e(x), w_e(x)$ given in (4.5) with $v_0 = \kappa_+$ is always unstable and $v_0 = \kappa_-$ is stable only when $0 < \gamma < \gamma_h$ for some $\gamma_h > 0$. As γ increases past γ_h, a Hopf bifurcation in the amplitudes of the spikes can be triggered.

Similar to §4(c), we can compute θ_h numerically by discretizing the NLEP (4.28*a*) using the finite difference method. Note that here θ_h depends on τ. See figure 4*b*, where we choose $\tau = 1$, and compute γ_h numerically for fixed $\hat{\theta}$ such that $Re(\lambda) = 0$.

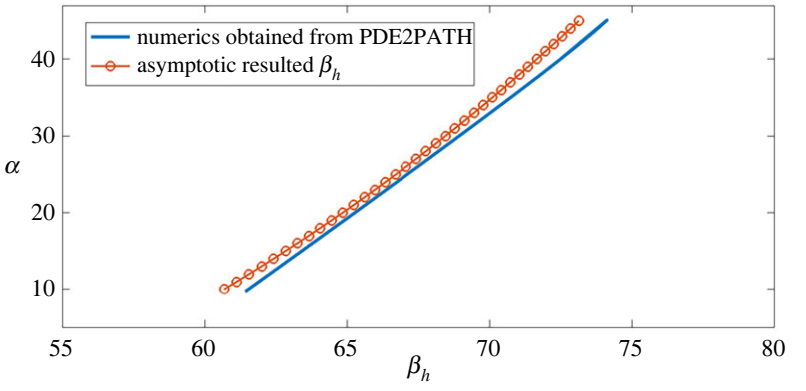

Figure 6. Comparison between asymptotic result and full simulations obtained from PDE2PATH for Hopf bifurcation threshold β_h. The parameters are $\delta_1 = 0.01, l = 100, \tau = 1, \theta = 1, c = 0.2, d = 1$.

(e) Numerical verification when $\theta = \tau = 1$

In this section, we verify our asymptotic results for Hopf bifurcation with numerical simulation. As this paper mainly considers system (4.1) with $l \to \infty$ and the time scaling $\tau = \theta = 1$, we then have $\hat{\theta} = 1/\delta_1^2\alpha^2$ and $\chi(\lambda)$ becomes $\chi(\lambda) = \lambda(1 + (c/(\lambda + d)))$.

We now validate result 4.6 with the data obtained from the continuation package PDE2PATH. For the fixed value of the parameters δ_1, α, c and d, we compute the critical bifurcation value for γ_h by discretizing the NLEP (4.28*a*) such that the real part of the largest eigenvalue crosses 0. This yields $\kappa_h = \sqrt{\gamma_h}/\delta_1^{1/4}\alpha^{1/2}$ from (4.31). Then substituting κ into the quadratic equation (3.19), we obtain the critical value β_h that triggers the Hopf bifurcation. Note that in the limit $\delta_1 \to 0$, $\delta_1\beta$ can be ignored and we obtain an explicit formula for β_h

$$\beta_h = \alpha\kappa_h + \frac{3}{\sqrt{\delta_1}\kappa_h}. \tag{4.32}$$

In figure 6, we compare the critical values β_h with the numerical data obtained from PDE2PATH. Here, we take the parameter value $\delta_1 = 0.01$, which is not very small, therefore, after obtaining κ_h, β_h is computed through the quadratic equation (3.15), which includes the higher order term $\delta_1\beta$ for better approximation. It is shown in figure 6 that the theory agrees pretty well with numerics.

Equation (4.32) provides the critical value of β at which Hopf bifurcation occurs in the limit $\delta_1 \to 0$ when $\tau = \theta = 1$. However, it does not say anything about the nature of Hopf bifurcation (subcritical or supercritical). This motivates the need to identify the Hopf bifurcation in the following §§5 and 6.

5. Subcritical breathing Hopf bifurcation

We further analyse the stability of the localized patterns examining the existence of breathing Hopf bifurcation. To determine the stability, we use PDE2PATH continuation package and the linear operator of the inhomogeneous problem by adopting the method developed in [22]. Thereby, we acquire the discretized matrix characterizing the linear operator of the localized pattern's solution. Then using a numerical solver, the eigenvalues of the spectrum are computed. Figure 7*a* plots the breathing Hopf bifurcation, which occurs at the left corner of the localized patterns region for the given values of parameters. The curve is obtained using PDE2PATH by continuing a Hopf point in two-parameter space. Note that the breathing Hopf curve shown in figure 7*a* corresponds to the blue curve in figure 6 with the parameter scaling $b = \delta_1\beta$ and $a = \delta_1\alpha$.

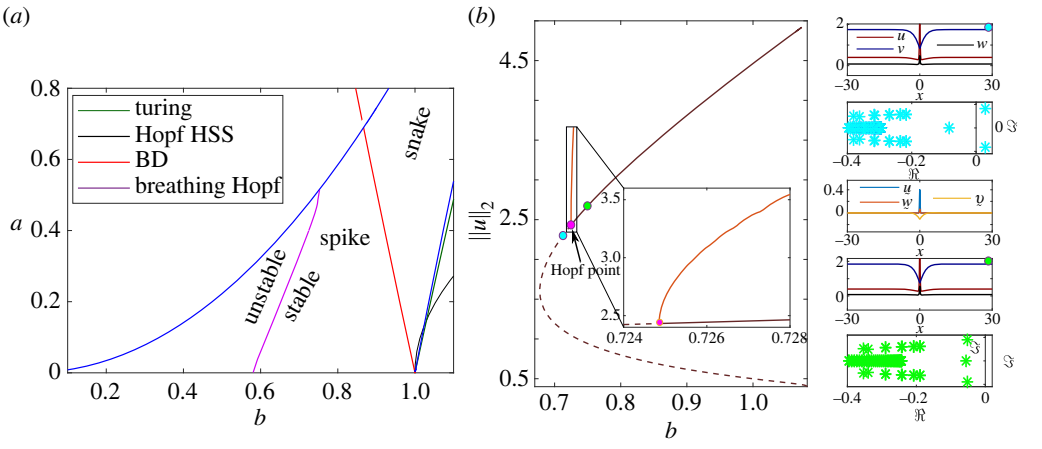

Figure 7. A zoom of the spike region with $\delta_1 = 0.01$, $c = 0.2$ and $d = 1$ in the limit $l = 100$. (*a*) The magenta curve indicates the breathing Hopf bifurcation. (*b*) Bifurcation diagram of vector max u versus d for fixed $a = 0.4$, showing the stable and unstable branches joining at the Hopf point $b_h = 0.7249$. The inserts plot the continuations of the periodic solution and represent solutions and the corresponding linear spectrum stability.

Figure 7*b* illustrates that the fold of one parameter continuation in the spike region becomes stable after the Hopf point rather than after the fold point as shown in figure 1*c* in which the value of a is outside the unstable region. In the panels on the right, we provide examples of stable and unstable solutions with linear spectrum stability and eigenvector closed to the Hopf bifurcation point. Observe that the eigenvectors are spatially localized, indicating that the Hopf bifurcation is the breathing mode of the spike.

Finally, we investigate the sub-supercritical Hopf bifurcation by continuations of the periodic solution using PDE2PATH. We trace the branch of periodic solutions emanating from the Hopf bifurcation point and we find it bifurcates subcritically; see the zoom in figure 7*b*. Therefore, the Hopf bifurcation for this value of δ_1 is subcritical.

6. Supercritical breathing Hopf bifurcation

Figure 8*a* displays similar findings to those in figure 7, but with an increased diffusion ratio of $\delta_1 = 0.05$. When comparing both figures, it is evident that with a lower δ_1, the breathing Hopf bifurcation curve impacts mainly the spike region's edge. However, at a higher δ_1, this curve crosses the BD curve, thereby affecting the homoclinic snaking zone. Additionally, at $\delta_1 = 0.05$, a fold in the Hopf bifurcation curve indicates two distinct Hopf instability branches. To validate this, a one-parameter continuation was performed, passing through both sides of the Hopf bifurcation branches. The outcomes, depicted in figure 8*b*, show the homoclinic snaking branches undergoing alterations due to two Hopf bifurcations, with an increase in instability as one progresses up these branches. To decode these Hopf bifurcations, PDE2PATH was employed to track the periodic solutions stemming from each bifurcation point. In order to understand the nature of these Hopf bifurcations, we again use PDE2PATH to trace the branch of periodic solutions that emanate from each Hopf bifurcation point. In the snaking diagram, the yellow curve showcases the continuation results, highlighting the dynamics of two distinct Hopf bifurcations. The periodic branch that originates from the first Hopf point, indicated by black dots within the snaking branch, undergoes a supercritical bifurcation. It then converges with the periodic branch emanating from the second Hopf point, marked by red dots on the snaking branch, which bifurcates subcritically. This configuration in the snaking diagram clearly illustrates the two types of Hopf bifurcations: a supercritical bifurcation occurring on the left side and a subcritical bifurcation on the right side. A sample solution at the cyan dot is shown in

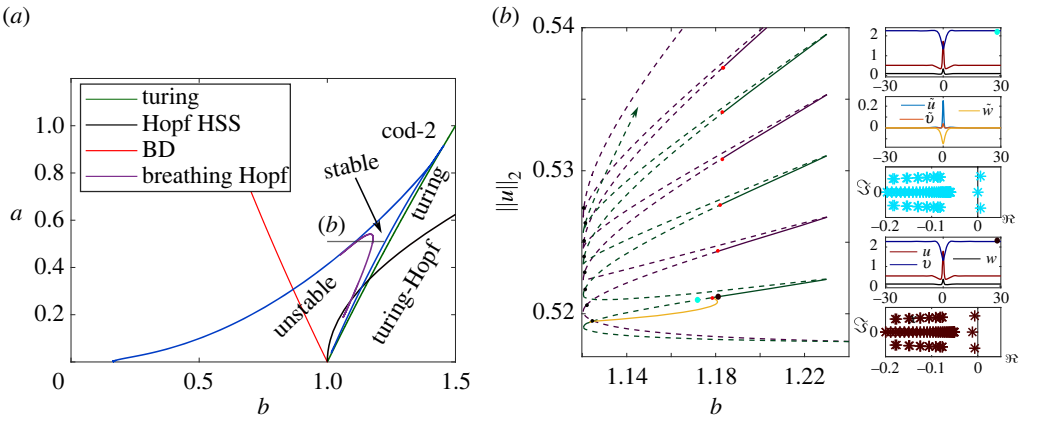

Figure 8. (*a*) The figure illustrates the same bifurcation diagram as in figure 1 for model (1.1) for $\delta_1 = 0.05$, with the location of Hopf bifurcations superimposed. (*b*) An example of one parameter continuation in b within the snaking. The maroon curve within the snaking diagram represents the continuation from the Hopf point. See text for details.

the top three panels. The first panel displays both localized solutions in variables u and v. The second panel exhibits the leading eigenvalues, which are complex and have a positive real part, signifying instability. The third panel illustrates the localized eigenvectors related to these leading eigenvalues, indicating a breathing-type instability. The two lower panels feature a solution at the brown dot. The fourth panel presents the localized solutions in u and v, while the fifth panel displays the leading eigenvalues, which in this case have a negative real part, denoting stability.

Moreover, at this particular value of δ_1, something noteworthy is observed in the system's behaviour. The Hopf bifurcation of the (HSS), depicted by the black curve in figure 8, extends beyond the Turing region and progresses into the region of localized states. This transition is significant as it indicates the onset of additional instabilities in the localized state region.

Two specific values of the parameter b were selected from the odd branch of the snaking diagram shown in figure 8, focusing on areas close to the Hopf bifurcation. These values were used to create figure 9. The parameter and initial conditions were meticulously chosen to ensure that b was slightly beyond the Hopf bifurcation, as depicted in plots (*a*), and a bit further past the bifurcation point, as seen in plots (*b*). The outcomes of these simulations are displayed in two formats: a heat map (on the left) and a time series of u-values at a specific point in the domain (on the right). These results suggest the presence of a stable limit cycle for the value of b that is just past the bifurcation point. This limit cycle, which appears as a 'breather' solution in the heat map, modulates the amplitude across the domain but is confined to a narrow range of parameters. Additionally, as b progresses beyond the Hopf bifurcation, the oscillation amplitude varies rapidly. For instance, figure 9*a* shows a solution with three patches, and figure 9*b* illustrates that crossing this secondary instability leads to spatio-temporal chaos.

In figure 10*a*, stability results are presented for an increased diffusion ratio of $\delta_1 = 0.07$. When compared with figure 8, it is apparent that the breathing Hopf bifurcation has moved up and to the right, resulting in the localized region becoming unstable with the exception of the tiny portion that is stable beyond the (magenta) breathing Hopf bifurcation. Figure 10*b* displays one parameter continuation of the snaking bifurcation diagram for $a = 0.6$ from the stable region. Here, we observe that, despite the primary branches being stable, a sequence of breathing Hopf bifurcations (black dots) causes instability in the branches of the snake associated with higher pulses. The insets in figure 10*b* illustrate the continuation of the periodic solution suggesting that the Hopf bifurcation is supercritical at this value of δ_1. Where the panels on the right represent samples of unstable and stable solutions.

For $\delta_1 > 0.07$, the localized pattern region is completely unstable as it is affected by a breathing-mode Hopf bifurcation, as well as an HSS Hopf instability (figure not shown).

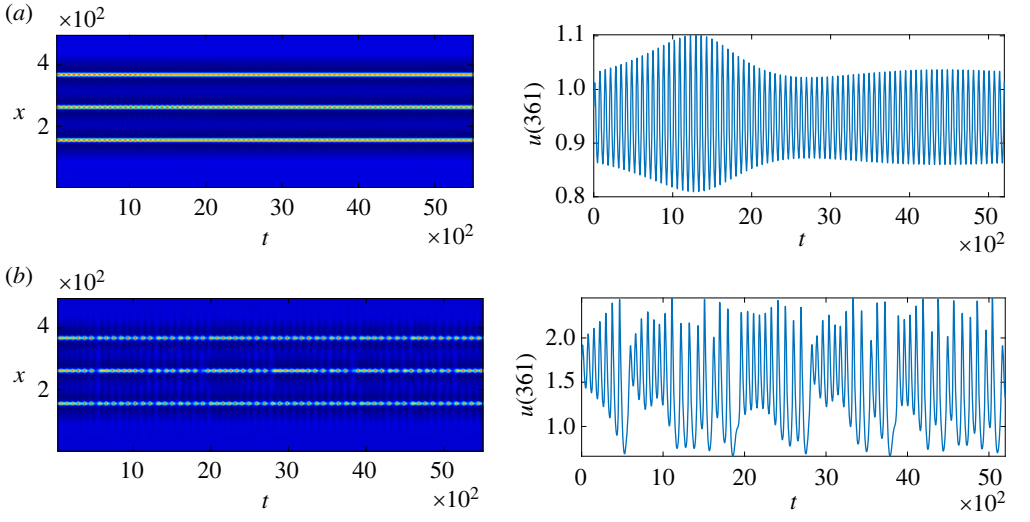

Figure 9. Using the direct numerical simulation of (1.1), the plot shows the space–time distribution of the u-component for $a = 0.5$ and two values of b. (*a*) For $b = 1.168$, just beyond the Hopf bifurcation, (*b*) For $b = 1.16$, a little further beyond the Hopf bifurcation. Other parameter values: as in figure 8.

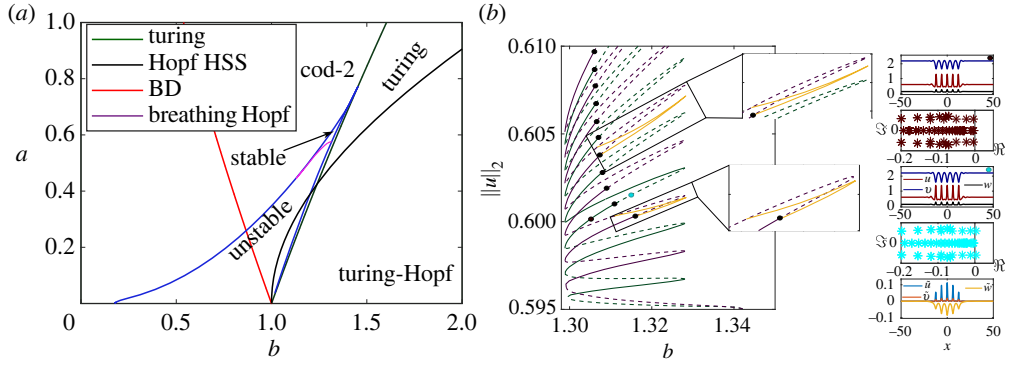

Figure 10. (*a*) The figure illustrates the same bifurcation diagram as in figure 1 for model (1.1) for $\delta_1 = 0.07$, with the location of Hopf bifurcations superimposed. (*b*) An example of one parameter continuation in b within the snaking. The two zooms present the continuation from the Hopf point. See text for details.

7. Conclusion

In this work, we investigated the connection between homoclinic snaking and semi-strength interaction by studying a three-variable reaction diffusion system—the extended Brusselator model for the BZ-AOT system.

We begin by performing linear stability to determine the conditions for Turing instability, Hopf bifurcation and BD transitions. The BD curve divides the localized structures region into two subregions: spikes and snakings. The spike region has pure real spatial eigenvalues, whereas the snaking region has complex spatial eigenvalues. Furthermore, we use weakly nonlinear analysis to determine the codimension-two point at which the Turing bifurcation changes from subcritical to supercritical. As the transition point appears, it indicates the emergence of a localized structure region, where localized solutions are found (spike and snaking).

We explore the localized structure region and found the presence of a Hopf bifurcation in the regime that the source parameters $a = O(\delta_1)$ and $b = O(\delta_1)$. Under this regime, singular

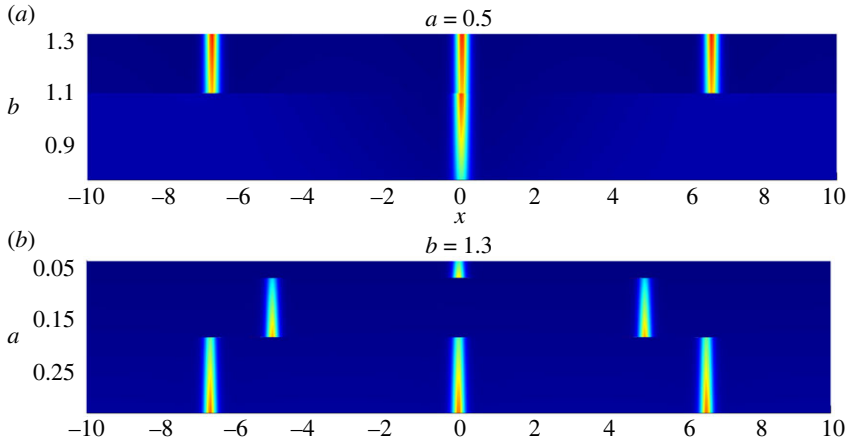

Figure 11. Spike insertion and spike annihilation. (*a*) Full simulations of (1.1) with $a = 0.5$ and with b gradually increased according to the formula $b = 0.8 + 0.0001 * t$; (*b*) Full simulations of (1.1) with $b = 1.3$ and with a gradually decreased according to the formula $a = 0.3 - 0.0001 * t$. The other parameters are $\delta_1 = 0.01, l = 10, c = 0.2, d = 1$.

perturbation techniques are applied to construct steady-state localized patterns. The theory predicts a fold point that connects two branches of spike solutions. Then non-local eigenvalue arguments show that the upper branch κ_+ is always unstable, while the stable lower branch can be destabilized through a Hopf bifurcation as b increases.

Finally, we have shown that in the corner of the spike region there is a breathing Hopf bifurcation for small diffusion ratios δ_1. PED2PATH is then used to demonstrate the subcritical nature of this Hopf bifurcation. By increasing the diffusion ratio δ_1, the extent of the breathing Hopf bifurcation eventually extends to encompass most of the localized structure region. Moreover, we observe that the Hopf bifurcation has changed from a subcritical to a supercritical bifurcation.

Studies in three-component reaction diffusion systems have shown that new dynamics can be introduced by the third component and have not been seen in typical two-component models [13,26–28]. For example, intricate nucleation-annihilation dynamics are studied in a three-component RD model of urban crime [28], and complex oscillatory dynamics of spike patterns are studied in a three-component Schnakenberg system [13]. In this paper, we show how homoclinic snaking theory and semi-strong interaction theory can be integrated for a three-component reaction–diffusion system, which leads to richer dynamical behaviours such as additional bifurcations and chaotic dynamics. Moreover, we extended the studies for the non-local-eigenvalue from the effect of one reaction time parameter to two, and a formula for the Hopf bifurcation threshold was derived in terms of the two reaction time parameters.

Numerous possible extensions of this model (1.1) are possible for future study. One open problem is to study the dynamics of spike patterns on a finite domain. In the semi-strong regime (singular limit of a large diffusivity ratio), it is well known that spike patterns can exhibit a variety of instabilities such as temporal oscillations in the height of the spikes, spike annihilation events, and spike self-replication. There is a rather well-developed theory to analyse the stability and dynamics of the spike patterns in a variety of specific RD systems such as the Gierer–Meinhardt [23–25,29], Schnakenberg [30] and Brusselator models [31]. In figure 11, we have performed further simulations of what can happen on a finite domain $l = 10$, and two types of instabilities are observed. In figure 11*a*, new spikes appear from the 'background' away from other spikes as b is increased. This is referred to as 'spike insertion' events. Contrast with spike replication, where a spike splits into two, this is a new mechanism that leads to the birth of new spikes. In figure 11*b*, some of the hot-spots get killed as a is decreased, resulting in fewer hot-spots.

Ethics. There are no ethical considerations to this research.
Data accessibility. There are no new data. All graphs show numerical results for the models presented.
Declaration of AI use. We have not used AI-assisted technologies in creating this article.
Authors' contributions. F.A.S.: formal analysis, investigation, software, writing—original draft, writing—review and editing; C.G.: formal analysis, investigation, resources, supervision, writing—original draft, writing—review and editing; M.N.: supervision, writing—original draft, writing—review and editing.

All authors gave final approval for publication and agreed to be held accountable for the work performed therein.
Conflict of interest declaration. We declare we have no competing interests.
Funding. F.A.S. has received travelling fund from Military Technological College.
Acknowledgements. The authors extend their gratitude for insightful discussions with Alan Champneys from the University of Bristol and Michael Ward from the University of British Columbia.

Appendix A

In this appendix, we prove lemma 4.2. First, we rewrite equation (4.25) as a quadratic equation in terms of λ

$$\lambda^2 + (c + \hat{d} - \chi)\lambda - \chi\hat{d} = 0, \tag{A 1}$$

in which $\hat{d} := d/\tau > 0$. This equation has two roots

$$\lambda_\pm = \frac{-(c + \hat{d} - \chi) \pm \sqrt{(c + \hat{d} - \chi)^2 + 4\chi\hat{d}}}{2}. \tag{A 2}$$

When χ is real and positive, the discriminant $(c + \hat{d} - \chi)^2 + 4\chi\hat{d}$ is positive, so the two roots $\lambda_\pm$ are real and $\lambda_+\lambda_- = -\chi d < 0$. Therefore, there exists a positive real λ when $\chi > 0$.

When χ is real and negative, then the two roots $\lambda_\pm$ could be real or complex. In the case where the roots are real, it is obvious to see $\lambda_- = (-(c + \hat{d} - \chi) - \sqrt{(c + \hat{d} - \chi)^2 + 4\chi\hat{d}})/2 < 0$; since $\chi < 0$, we have $(c + \hat{d} - \chi)^2 > (c + \hat{d} - \chi)^2 + 4\chi\hat{d}$, so $\lambda_+ = (-(c + \hat{d} - \chi) + \sqrt{(c + \hat{d} - \chi)^2 + 4\chi\hat{d}})/2$ is also negative. In the case where the two roots are complex, $\lambda_+ + \lambda_- = 2Re(\lambda) = -(c + \hat{d} - \chi) < 0$. Therefore, equation (A 1) has either two negative real roots or two complex roots with negative real part when $\chi < 0$.

Now we consider the case that χ is complex and write $\chi = \chi_R + i\chi_I$. To prove part (b) of lemma 1, we let $\chi_R < 0$. Then introducing the notation $m := c + \hat{d} - \chi_R > 0$, the root formula (A2) becomes

$$\begin{aligned}\lambda_\pm &= \frac{1}{2}\left(-m + i\chi_I \pm \sqrt{(m - i\chi_I)^2 + 4\chi_R\hat{d} + 4i\chi_I\hat{d}}\right)\\ &= \frac{1}{2}\left(-m + i\chi_I \pm \sqrt{a + ib}\right),\end{aligned} \tag{A 3}$$

where $a = m^2 - \chi_I^2 + 4\chi_R\hat{d}$ and $b = 2\chi_I(2\hat{d} - m)$. To compute the square root of complex number $a + bi$, we let $a + ib = (x + iy)^2$, which yields two equations in terms of x, y

$$x^2 - y^2 = a \quad \text{and} \quad 2xy = b.$$

Solving for x, y using these two equations, we obtain that

$$\sqrt{a + ib} = \pm\left(\sqrt{\frac{|z| + a}{2}} + i\frac{b}{|b|}\sqrt{\frac{|z| - a}{2}}\right), \tag{A 4}$$

where $|z| = \sqrt{a^2 + b^2}$. Then substituting (A 4) into (A 3), we get

$$\lambda_\pm = \frac{1}{2}\left(-m \pm \sqrt{\frac{|z| + a}{2}}\right) + i\frac{1}{2}\left(\chi_I \pm \frac{b}{|b|}\sqrt{\frac{|z| - a}{2}}\right). \tag{A 5}$$

We are interested in the real parts of the two roots, which is

$$Re(\lambda_{\pm}) = \frac{1}{2}\left(-m \pm \sqrt{\frac{|z|+a}{2}}\right).$$

Since $|z| = \sqrt{a^2+b^2} > |a|$, we have $\sqrt{(|z|+a)/2} > 0$ so $Re(\lambda_-) = (1/2)(-m - \sqrt{(|z|+a)/2}) < 0$. For the other root, to show that $Re(\lambda_-) = (1/2)(-m + \sqrt{(|z|+a)/2}) < 0$, we want to show $-m + \sqrt{(|z|+a)/2} < 0$ or

$$2m^2 - a > |z|. \tag{A 6}$$

Since $a = m^2 - \chi_I^2 + 4\chi_R\hat{d} < m^2 < 2m^2$, we square both sides of (A 6) and it is equivalent to prove

$$4m^4 - 4m^2 a - b^2 > 0. \tag{A 7}$$

Now we substitute $m = c + \hat{d} - \chi_R$, $a = m^2 - \chi_I^2 + 4\chi_R\hat{d}$ and $b = 4\chi_I\hat{d} - 2m\chi_I$ into (A 7) and obtain that

$$-m^2\chi_R + \chi_I^2(m - \hat{d}) > 0, \tag{A 8}$$

which is obviously true when $\chi_R < 0$. Therefore, $Re(\lambda_{\pm}) < 0$ whenever $\chi_R < 0$. Note that equation (A 8) is still true when $\chi_R = 0$ and $\chi_I \neq 0$. This completes the proof of lemma 4.2.

References

1. Epstein I. 1984 Complex dynamical behavior in 'simple' chemical systems. *J. Phys. Chem.* **88**, 187–198. (doi:10.1021/j150646a007)
2. Vanag V, Epstein I. 2001 Pattern formation in a tunable medium: the Belousov-Zhabotinsky reaction in an aerosol OT microemulsion. *Phys. Rev. Lett.* **87**, 228301 (doi:10.1103/PhysRevLett.87.228301)
3. Vanag VK, Epstein IR. 2001 Pattern formation in a tunable medium: the Belousov-Zhabotinsky reaction in an aerosol OT microemulsion. *Phys. Rev. Lett.* **87**, 228301. (doi:10.1103/PhysRevLett.87.228301)
4. Dähmlow P, Vanag VK, Müller SC. 2014 Effect of solvents on the pattern formation in a Belousov-Zhabotinsky reaction embedded into a microemulsion. *Phys. Rev. E* **89**, 010902. (doi:10.1103/PhysRevE.89.010902)
5. Yang L, Dolnik M, Zhabotinsky A, Epstein I. 2002 Pattern formation arising from interactions between Turing and wave instabilities. *J. Chem. Phys.* **117**, 7259–7265. (doi:10.1063/1.1507110)
6. Prigogine I, Lefever R. 1968 Symmetry breaking instabilities in dissipative systems. II. *J. Chem. Phys.* **48**, 1695–1700. (doi:10.1063/1.1668896)
7. Field R, Noyes R. 1974 Oscillations in chemical systems. IV. Limit cycle behavior in a model of a real chemical reaction. *J. Chem. Phys.* **60**, 1877–1884. (doi:10.1063/1.1681288)
8. Schneider TM, Marinc D, Eckhardt B. 2010 Localized edge states nucleate turbulence in extended plane Couette cells. *J. Fluid Mech.* **646**, 441–451. (doi:10.1017/S0022112009993144)
9. Batiste O, Knobloch E, Alonso A, Mercader I. 2006 Spatially localized binary-fluid convection. *J. Fluid Mech.* **560**, 149–158. (doi:10.1017/S0022112006000759)
10. Laing CR, Troy WC, Gutkin B, Ermentrout GB. 2002 Multiple bumps in a neuronal model of working memory. *SIAM J. Appl. Math.* **63**, 62–97. (doi:10.1137/S0036139901389495)
11. Korteweg DDJ, de Vries DG. 1895 XLI. On the change of form of long waves advancing in a rectangular canal, and on a new type of long stationary waves. *Lond., Edinb. Dublin Phil. Mag. J. Sci.* **39**, 422–443. (doi:10.1080/14786449508620739)
12. Yochelis A, Tintut Y, Demer LL, Garfinkel A. 2008 The formation of labyrinths, spots and stripe patterns in a biochemical approach to cardiovascular calcification. *New J. Phys.* **10**, 055002. (doi:10.1088/1367-2630/10/5/055002)
13. Xie S, Kolokolnikov T, Nishiura Y. 2021 Complex oscillatory motion of multiple spikes in a three-component Schnakenberg system. *Nonlinearity* **34**, 5708. (doi:10.1088/1361-6544/ac0d46)
14. Tse WH, Ward MJ. 2018 Asynchronous instabilities of crime hotspots for a 1-D reaction-diffusion model of urban crime with focused police patrol. *SIAM J. Appl. Dyn. Syst.* **17**, 2018–2075. (doi:10.1137/17M1162585)

15. Buttenschoen A, Kolokolnikov T, Ward MJ, Wei J. 2020 Cops-on-the-dots: the linear stability of crime hotspots for a 1-D reaction-diffusion model of urban crime. *Eur. J. Appl. Math.* **31**, 871–917. (doi:10.1017/S0956792519000305)
16. Gai C, Kolokolnikov T. 2021 Resource-mediated competition between two plant species with different rates of water intake.
17. Cross M, Hohenberg P. 1993 Pattern formation outside of equilibrium. *Rev. Mod. Phys.* **65**, 851–1112. (doi:10.1103/RevModPhys.65.851)
18. Breña–Medina V, Champneys A. 2014 Subcritical Turing bifurcation and the morphogenesis of localized patterns. *Phys. Rev. E* **90**, 032923. (doi:10.1103/PhysRevE.90.032923)
19. Uecker H. 2017 Hopf bifurcation and time periodic orbits with pde2path – algorithms and applications. *Commun. Comput. Phys.* **25**, 812–852. (doi:10.4208/cicp.OA-2017-0181)
20. Uecker H. 2021 *Numerical continuation and bifurcation in nonlinear PDEs*. Philadelphia, PA: Society for Industrial and Applied Mathematics.
21. Al Saadi F, Champneys A, Gai C, Kolokolnikov T. 2022 Spikes and localised patterns for a novel Schnakenberg model in the semi-strong interaction regime. *Eur. J. Appl. Math.* **33**, 133–152. (doi:10.1017/S0956792520000431)
22. Al Saadi F, Champneys A, Verschueren van Rees N. 2021 Localized patterns and semi-strong interaction, a unifying framework for reaction-diffusion systems. *IMA J. Appl. Math.* **86**, 1031–1065. (doi:10.1093/imamat/hxab036)
23. Iron D, Ward MJ, Wei J. 2001 The stability of spike solutions to the one-dimensional Gierer–Meinhardt model. *Physica D* **150**, 25–62. (doi:10.1016/S0167-2789(00)00206-2)
24. Ward MJ, Wei J. 2003 Hopf bifurcations and oscillatory instabilities of spike solutions for the one-dimensional Gierer-Meinhardt model. *J. Nonlinear Sci.* **13**, 209–264. (doi:10.1007/s00332-002-0531-z)
25. Wei J. 1999 On single interior spike solutions of the Gierer–Meinhardt system: uniqueness and spectrum estimates. *Eur. J. Appl. Math.* **10**, 353–378. (doi:10.1017/S0956792599003770)
26. Nishiura Y, Teramoto T, Yuan X. 2011 Heterogeneity-induced spot dynamics for a three-component reaction-diffusion system. *Commun. Pure Appl. Anal.* **11**, 307–338. (doi:10.3934/cpaa.2012.11.307)
27. Gai C, Iron D, Kolokolnikov T. 2020 Localized outbreaks in an SIR model with diffusion. *J. Math. Biol.* **80**, 1389–1411. (doi:10.1007/s00285-020-01466-1)
28. Gai C, Ward M. 2023 The nucleation-annihilation dynamics of hotspot patterns for a reaction-diffusion system of urban crime with police deployment. submitted to SIADS (37 p).
29. Doelman A, Gardner RA, Kaper TJ. 2001 Large stable pulse solutions in reaction-diffusion equations. *Ind. Univ. Math. J.* **50**, 443–507. (doi:10.1512/iumj.2001.50.1873)
30. Ward MJ, Wei J. 2002 The existence and stability of asymmetric spike patterns for the Schnakenberg model. *Stud. Appl. Math.* **109**, 229–264. (doi:10.1111/1467-9590.00223)
31. Tzou J, Nec Y, Ward M. 2013 The stability of localized spikes for the 1-D Brusselator reaction–diffusion model. *Eur. J. Appl. Math.* **24**, 515–564. (doi:10.1017/S0956792513000089)